Research
A SCIENCE PARTNER JOURNAL

RESEARCH ARTICLE

Bi-Doped Pd Aerogels with Tensile-Strain-Induced Cascade Orbital Hybridization Boost H_2O_2 Selective Activation for Efficient Pesticide Distinction

Ruimin Li[1,2†], Chengjie Chen[1†], Lijun Hu[1], Dongbo Yan[1], Xiaotong Li[1], Xiangkun Jia[1], Yu Wu[2], Lei Jiao[1*], Yanling Zhai[1*], and Chengzhou Zhu[2*]

[1]Institute of Molecular Metrology, College of Chemistry and Chemical Engineering, Qingdao University, Qingdao 266071, P. R. China. [2]State Key Laboratory of Green Pesticide, International Joint Research Center for Intelligent Biosensing Technology and Health, College of Chemistry, Central China Normal University, Wuhan 430079, P. R. China.

*Address correspondence to: jiaolei@qdu.edu.cn (L.J.); zhaiyanling@qdu.edu.cn (Y.Z.); czzhu@ccnu.edu.cn (C.Z.)
†These authors contributed equally to this work.

Citation: Li R, Chen C, Hu L, Yan D, Li X, Jia X, Wu Y, Jiao L, Zhai Y, Zhu C. Bi-Doped Pd Aerogels with Tensile-Strain-Induced Cascade Orbital Hybridization Boost H_2O_2 Selective Activation for Efficient Pesticide Distinction. *Research* 2026;9:Article 1300. https://doi.org/10.34133/research.1300

Submitted 4 February 2026
Revised 1 May 2026
Accepted 11 May 2026
Published 5 June 2026

Copyright © 2026 Ruimin Li et al. Exclusive licensee Science and Technology Review Publishing House. No claim to original U.S. Government Works. Distributed under a Creative Commons Attribution License (CC BY 4.0).

The selective activation of H_2O_2 into hydroxyl radicals (•OH) through the synergistic interplay between the nanozyme's internal orbital interactions and external orbital coupling with intermediates presents an important scientific challenge. In this study, we demonstrate that PdBi aerogels with controllable tensile strain first enhance the Pd d orbital energy level through p–d orbital hybridization, and subsequently, the hybridized Pd d orbitals couple sequentially with the molecular orbitals of H_2O_2, forming a cascade of orbital hybridizations. High-performance liquid chromatography quantitative analysis reveals that the engineered PdBi aerogels remarkably improve •OH selectivity from 73.3% to 95.4%, importantly boosting both the activation efficiency and selectivity. Experimental studies and theoretical calculations have demonstrated that the hybridization of the d orbitals of Pd and the p orbitals of Bi in PdBi aerogels initially raises the d-band energy level of the Pd atoms. During the activation of H_2O_2, the high-energy $4d_{xz/yz}$ and $4d_{z^2}$ orbitals of Pd further hybridize with the $2\pi^*$ and 5σ orbitals of H_2O_2, thereby enhancing the orbital interaction with H_2O_2 and creating optimal conditions for O–O bond cleavage and consequently enhancing the efficiency of •OH generation. Capitalizing on the differential reactivity patterns of various pesticides with PdBi aerogels, we develop a colorimetric sensor array for the discrimination and simultaneous detection of pesticide residues. Taking chlorpyrifos as an example, the detection limit is 0.23 μM, demonstrating good detection sensitivity. This work presents an orbital-level design strategy for creating highly selective nanozymes in H_2O_2 activation systems.

Introduction

Hydrogen peroxide (H_2O_2) serves not only as an important reaction medium in environmental remediation and organic synthesis but also plays a pivotal role in biosensing and energy conversion [1–6]. However, the oxidizing capacity of H_2O_2 is inherently limited, necessitating efficient activation to convert it into reactive oxygen species (ROS) such as hydroxyl radicals (•OH), superoxide radicals ($•O_2^-$), and metal-oxo species (M=O) [7–9]. Among these, the •OH exhibits remarkable advantages in oxidizing organic compounds due to its extremely high redox potential and potent nonselective oxidizing capability, which can significantly amplify signals and thereby substantially enhance detection sensitivity [10,11]. Nevertheless, the spontaneous decomposition of H_2O_2 is inefficient. Its activation process heavily relies on catalyst performance. Among various strategies for activating H_2O_2, nanozymes, as a novel type of artificial catalyst, provide an effective approach to addressing the aforementioned issue due to their designable catalytic activity and controllable ROS-generating capacity. Therefore, the development of highly efficient nanozymes to achieve controllable •OH generation is crucial for improving both catalytic reaction efficiency and sensing performance.

To address these challenges, researchers have explored various regulation strategies, including interface engineering [12,13], dual-site engineering [14,15], and defect engineering [16,17]. While regulation strategies have improved H_2O_2 activation efficiency, precise control over the reaction pathway remains elusive [18]. The fundamental limitation originates from insufficient overlap between metal d orbitals and the σ orbitals of H_2O_2,

leading to inefficient O–O bond cleavage [19–21]. Although electronic structure modulation and the d-band center theory have been widely used to enhance catalytic activity, there is still a lack of effective strategies that can achieve site-specific orbital hybridization [22]. Notably, existing studies have shown that d–d, p–d, and f–p–d orbital hybridization can importantly improve catalytic performance; however, these strategies often focus on the internal orbital interactions within the nanozyme and frequently overlook the subsequent hybridization process between the catalytically active sites and the target molecules [23,24]. In fact, it is this cascade orbital hybridization with the adsorbates that has a decisive impact on the activity and selectivity of catalytic reactions. Therefore, precisely triggering and regulating this crucial subsequent cascade orbital hybridization process remains a significant challenge in current research.

Herein, we propose an effective cascade orbital hybridization strategy using Bi-doped Pd (PdBi) aerogels. The Bi-induced tensile strain in the Pd lattice triggers pronounced p–d orbital hybridization, which in turn modulates the hybridization between the d orbitals of the catalytic sites and the σ orbitals of H_2O_2, thus forming a p–d–σ cascade orbital hybridization. This electronic manipulation importantly enhances the p–d–σ hybridization between the nanozyme and H_2O_2, promoting the selective activation of H_2O_2 and increasing the •OH selectivity from 73.3% to 95.4%. Experimental and theoretical analyses confirm that p–d hybridization elevates the d-band center of Pd, facilitating cascade orbital interactions with H_2O_2. This promotes O–O bond elongation (from 1.489 to 1.508 Å) and efficient •OH formation. Capitalizing on the differential inhibition of •OH generation by various pesticides, we design a colorimetric sensor array for the precise identification and simultaneous quantification of pesticide residues. This work not only advances the fundamental understanding of orbital-level nanozyme design but also provides a practical platform for environmental monitoring applications.

Results and Discussion

Characterization of the nanozymes

PdBi hydrogels were synthesized through the reduction of palladium acetylacetonate [$Pd(acac)_2$] and bismuth (III) chloride ($BiCl_3$) with sodium borohydride (Fig. 1A). The aerogels were obtained via a freeze-drying process of the as-prepared hydrogels (inset in Fig. 1B) [25]. Subsequently, inductively coupled plasma atomic emission spectrometry analysis indicated that the atomic ratio of Pd to Bi in the PdBi aerogels is 100:5 (defined as $Pd_{100}Bi_5$ aerogels). Additionally, pure Pd aerogels and $Pd_{100}Bi_x$ (x = 2, 10) were prepared for comparison. This composition is consistent with the molar ratio used in the synthesis process (Table S1). As shown in Fig. 1B and C and Fig. S1, the morphology of the resulting Pd aerogels and $Pd_{100}Bi_5$ aerogels is investigated by scanning electron microscopy and transmission electron microscopy (TEM), revealing 3D architectures composed of interconnected porous and extended nanowire networks [26]. The high-resolution TEM (HR-TEM) result demonstrates that the $Pd_{100}Bi_5$ aerogels have a lattice spacing of 0.237 nm ascribed to the (111) planes of face-centered cubic Pd aerogels (Fig. 1D). Besides, the selected area electron diffraction (SAED) also reveals the polycrystalline nature of $Pd_{100}Bi_5$ aerogels, which are indexed to (111), (200), (220), and (311) of Pd (Fig. S2). The uniformly distributed Pd and Bi elements in the $Pd_{100}Bi_5$ aerogels are further demonstrated by the energy-dispersive x-ray spectroscopy mapping images (Fig. 1E). The x-ray diffraction pattern of Pd and PdBi aerogels reveals the face-centered cubic polycrystalline structure, consistent with the SAED results (Fig. 1F). In contrast to Pd aerogels, the reflections of PdBi aerogels exhibit noticeable shifts toward lower 2θ values as the fraction of Bi increases, which suggests that doping Bi into the Pd lattice can produce tensile strain [27]. Quantitative analysis based on the Bragg formula shows that this tensile strain increases from 0.52% to 1.29% as the Bi content increases (Fig. 1G). Additionally, the (111) lattice stripe spacing is directly measured by HR-TEM, and it is found that the lattice spacing of Pd is 0.232 nm. As the Bi-doping amount increases, the lattice spacing gradually increases, confirming the existence of the strain (Fig. S3). Notably, the continuous increase in this tensile strain suggests that we can precisely control the electronic structure of the Pd lattice by adjusting the amount of Bi doping.

Chemical state and electronic interaction

X-ray photoelectron spectroscopy (XPS) was performed to investigate the electronic structure and surface composition. With increasing Bi-doping concentration, a gradual decrease in the binding energy of Pd is observed, accompanied by a concurrent increase in the binding energy of Bi, indicating a clear electron transfer from Pd to Bi atoms (Fig. 2A). More importantly, in the Bi 4f spectra, 2 pairs of peaks are associated with Bi^0 and Bi^{3+} species. The relative content of Bi^{3+} shows a trend of increasing first, then decreasing, with increasing doping amount. This trend is crucial for understanding the aforementioned charge transfer behavior and its influence on catalytic performance. The Bi^{3+} species possess empty p orbitals, and their increased content importantly enhances the p–d orbital hybridization between Pd and Bi, thereby modulating the electronic interactions within the nanozyme. The XPS results provide direct evidence for the modulation of electronic structure in PdBi aerogels (Fig. 2B).

To verify the presence of orbital interaction between Pd and Bi, the projected density of states (PDOS) was calculated (Fig. 2C). The peaks of the Pd 4d orbitals align well with those of the Bi 6p orbitals, indicating strong p–d orbital hybridization. Based on the orbital symmetry, the d_z^2 orbital of Pd 4d can directionally hybridize with the p_z orbital of Bi 6p to form σ and σ* orbitals. Meanwhile, the $p_{x/y}$ orbitals of Bi 6p can directionally interact with the d_{xz}/d_{yz} orbitals of Pd 4d, generating π and π* orbitals (Fig. 2D and Fig. S4). Additionally, due to the mismatch in orbital orientation with the Bi 6p orbital, the d_{xy} and $d_{x^2-y^2}$ orbitals of Pd 4d are considered nonbonding. As shown in Fig. 2E and F, the p–d hybridization center on the orbitals leads to electron transfer from Bi to Pd, which can be verified through XPS spectra and differential charge density analysis. The crucial principle is that the lattice stretching strain caused by Bi doping (Fig. 1G) effectively promotes the occurrence of this p–d hybridization. With the assistance of the strain, the p–d hybridization between Pd and Bi not only induces charge transfer but also adjusts the symmetry and energy level distribution of the Pd d orbitals, thereby shifting the d-band center of Pd toward the Fermi level (Fig. 2G and Fig. S5). It is precisely this strain-induced p–d hybridization that directly regulates the local electronic structure of Pd, laying the foundation for the subsequent cascade orbital hybridization (p–d–σ) in the H_2O_2 activation process.

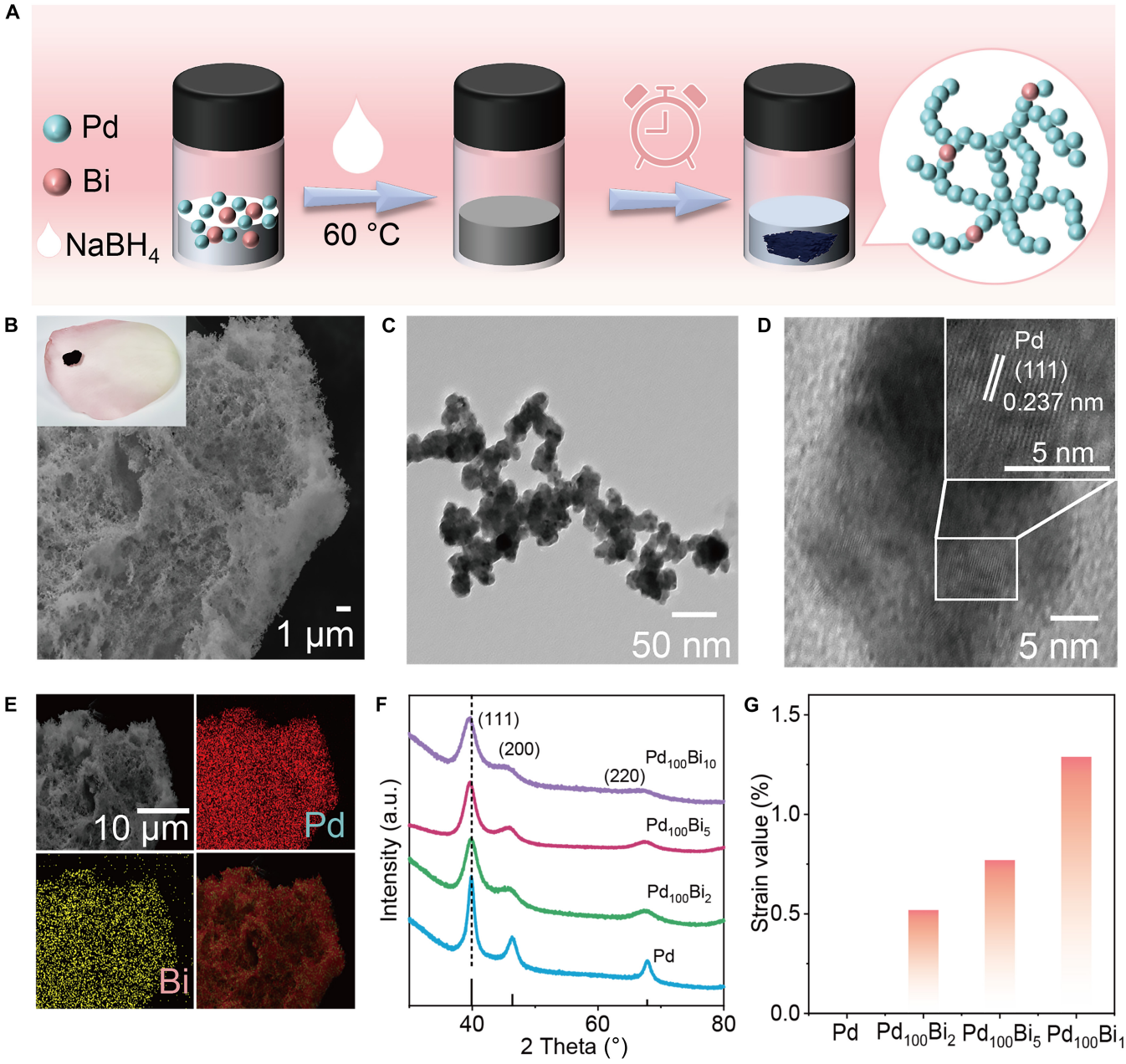


Fig. 1. (A) Schematic illustration of the synthesis of $Pd_{100}Bi_5$ aerogels. (B) Scanning electron microscopy image (inset: digital photograph of $Pd_{100}Bi_5$ aerogel). (C) Transmission electron microscopy (TEM) image. (D) High-resolution TEM image. (E) Energy-dispersive x-ray spectroscopy mapping images of $Pd_{100}Bi_5$ aerogels. (F) X-ray diffraction patterns of Pd and PdBi aerogels. (G) Strain value of Pd and PdBi aerogels.

Catalytic performance of nanozymes

The ability of $Pd_{100}Bi_x$ (x = 2, 5, 10) aerogels to activate H_2O_2 was examined using 3,3′,5,5′-tetramethylbenzidine (TMB) as a substrate, which is quantitatively assessed by measuring the absorbance of the oxidized form of TMB (oxTMB) at 652 nm [28,29]. As expected, $Pd_{100}Bi_x$ (x = 2, 5, 10) aerogels have a higher absorbance value than Pd aerogels, demonstrating excellent H_2O_2 activation ability, indicating that the p–d orbital hybridization of $Pd_{100}Bi_x$ (x = 2, 5, 10) aerogels plays a critical role in enhancing the H_2O_2 activation ability (Fig. 3A). Among them, $Pd_{100}Bi_x$ (x = 2, 10) aerogels are optimized for H_2O_2 activation. The specific activity (SA) is a quantitative measure of the H_2O_2-activation ability of $Pd_{100}Bi_x$ (x = 2, 5, 10) aerogels. $Pd_{100}Bi_5$ aerogels demonstrate a high SA value (751.1 U/mg), exceeding those of $Pd_{100}Bi_{10}$ (642.8 U/mg), $Pd_{100}Bi_2$ (161.4 U/mg), and Pd aerogels (107.6 U/mg) (Fig. 3B and Fig. S6). It should be pointed out that the $Pd_{100}Bi_{10}$ aerogels, despite having the largest tensile strain, exhibit a lower H_2O_2 activation performance (SA = 642.8 U/mg) compared with $Pd_{100}Bi_5$ (751.1 U/mg). This indicates that the simple strain effect is not sufficient to optimize the catalytic activity. We believe that the enhanced p–d orbital hybridization due to the moderate Bi doping plays a more crucial role in regulating the electrons, enhancing the H_2O_2 adsorption, and promoting the subsequent cascade hybridization at the core of the Pd d-band center. Besides, the kinetics of Pd and PdBi aerogels are evaluated using the

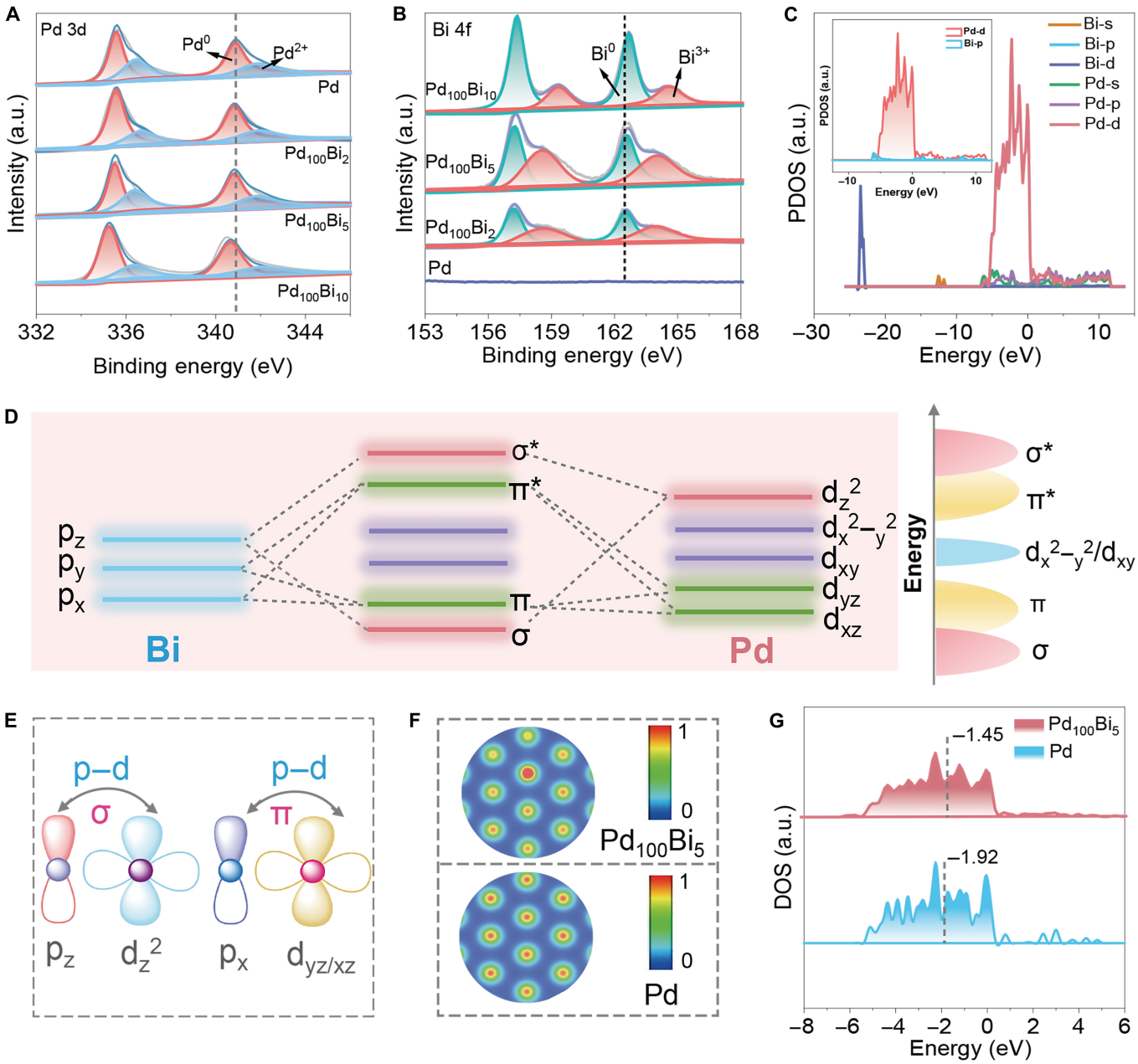


Fig. 2. (A) Pd 3d and (B) Bi 4f x-ray photoelectron spectroscopy (XPS) spectra of Pd and PdBi aerogels. (C) Projected density of states (PDOS) of $Pd_{100}Bi_5$ aerogels (the inset depicts a plot of the Pd 4d orbital and Bi 6p orbital). (D) The p–d orbital hybridization distribution pattern and the energy level of the Pd–Bi orbital hybridized density of states of $Pd_{100}Bi_5$ aerogels. (E) Schematic illustration of the hybridization between the p orbitals of Bi and the d orbitals of Pd. (F) The charge difference on the surface of Pd and Bi for $Pd_{100}Bi_5$ aerogels and Pd aerogels. Red and blue colors represent the depletion and accumulation of electrons, respectively. (G) The calculated d-band center of surface Pd for $Pd_{100}Bi_5$ aerogels and Pd aerogels.

Michaelis–Menten equation (Fig. S7 and Table S2). $Pd_{100}Bi_5$ aerogels exhibit lower K_m values and higher V_{max} values compared to $Pd_{100}Bi_x$ (x = 0, 2, 10), indicating stronger substrate affinity and superior catalytic performance. Then, cyclic voltammetry is performed to assess the catalytic efficiency of H_2O_2 using Pd and $Pd_{100}Bi_5$ aerogel-modified glassy carbon electrodes in an N_2-saturated acetate buffer. As shown in Fig. S8, $Pd_{100}Bi_5$ aerogels exhibit a notable reduction in current, indicating exceptional H_2O_2 reduction activity. To further reveal the mechanism of H_2O_2 activation enhanced by $Pd_{100}Bi_5$ aerogels, the activation energy (E_a) of H_2O_2 activation ability is compared using the Arrhenius equation [30]. The E_a value for the H_2O_2 activation of $Pd_{100}Bi_5$ aerogels (11.51 kJ/mol) is lower than $Pd_{100}Bi_{10}$ (17.50 kJ/mol), $Pd_{100}Bi_2$ (24.91 kJ/mol), and Pd aerogels (30.67 kJ/mol), indicating that $Pd_{100}Bi_5$ aerogels can more easily activate H_2O_2 (Fig. 3C). This value is comparable to those reported for other nanozymes, further confirming the excellent activation ability of $Pd_{100}Bi_5$ aerogels (Table S3). To achieve a more comprehensive understanding of the fundamental mechanism driving the enhanced H_2O_2 activation capability of $Pd_{100}Bi_5$ aerogels, the intermediates were investigated. A standard fluorescent probe, terephthalic acid, can capture •OH, yielding a fluorescent product with an emission peak at 440 nm. Upon the concurrent presence of $Pd_{100}Bi_5$

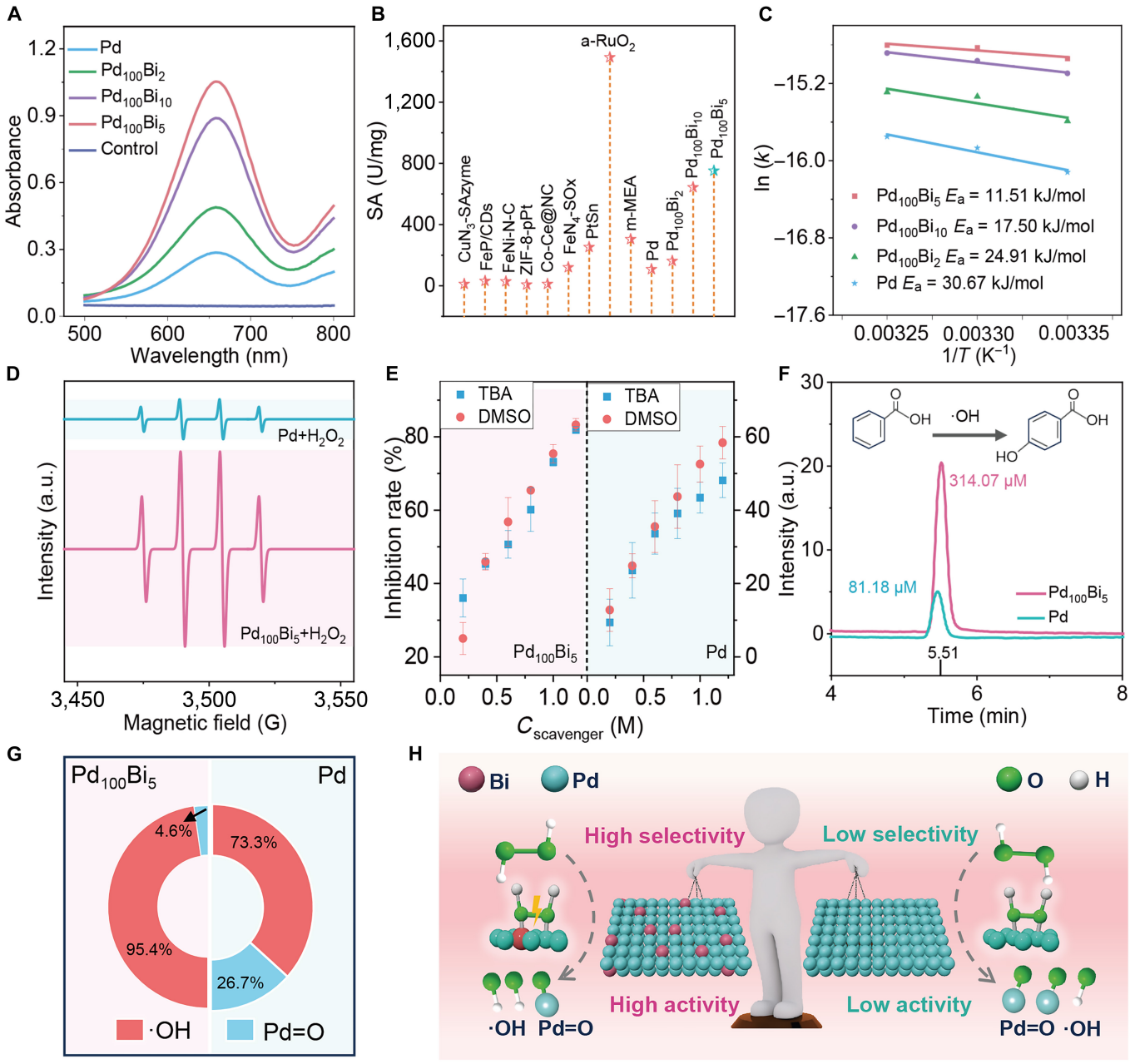


Fig. 3. (A) Absorbance spectra of the 3,3′,5,5′-tetramethylbenzidine/H_2O_2 system catalyzed by $Pd_{100}Bi_5$ and $Pd_{100}Bi_x$ (x = 0, 2, 10) aerogels. (B) The specific activity (SA) of the $Pd_{100}Bi_x$ (x = 0, 2, 5, 10) aerogels and the reported nanomaterials. CDs, carbon dots; NC, nitrogen-doped carbon; ZIF, zeolitic imidazolate framework; m-MEA, mesoporous medium-entropy alloy. (C) Arrhenius plots of ln(*k*) versus 1/*T* for H_2O_2 activation ability of $Pd_{100}Bi_x$ (x = 0, 2, 5, 10). E_a, activation energy. (D) 5,5-Dimethyl-1-pyrrolidine-*N*-oxide spin-trapping electron-paramagnetic-resonance spectra of Pd aerogels with H_2O_2 and $Pd_{100}Bi_5$ aerogels with H_2O_2. (E) The inhibited activity of both $Pd_{100}Bi_5$ and Pd systems after treatment with various concentrations of scavengers, including *tert*-butyl alcohol (TBA) and dimethylsulfoxide (DMSO). (F) Concentration of •OH concentration between the Pd and PdBi systems. The diagram illustrates the reaction mechanism of benzoic acid (BA) with •OH, resulting in the formation of *p*-hydroxybenzoic acid. (G) Selectivity of active intermediates in $Pd_{100}Bi_5$ and Pd-mediated H_2O_2 activation. (H) Schematic illustration of selective H_2O_2 activation on the $Pd_{100}Bi_5$ aerogels.

aerogels, H_2O_2, and terephthalic acid, a conspicuous fluorescence signal emerges, affirming the presence of •OH intermediates (Fig. S9). Electron-paramagnetic-resonance measurements applying 5,5-dimethyl-1-pyrrolidine-*N*-oxide (DMPO) as the spin-trapping agent were further performed, as shown in Fig. 3D. The $Pd_{100}Bi_5$ aerogels–H_2O_2 system exhibits a more pronounced DMPO–•OH signal than Pd aerogels, indicating that $Pd_{100}Bi_5$ aerogels activate H_2O_2 to generate more •OH. Based on this, to comprehensively determine whether there are other types of ROS in the system, using DMPO and 2,2,6,6-tetramethylpiperidinooxy as traps, respectively, no characteristic signals of superoxide anion radicals ($•O_2^-$) and singlet oxygen ($^1O_2$) were detected, thereby excluding the interference of these 2 common ROS (Fig. S10). In addition, in situ Fourier-transform infrared spectroscopy is used to verify the changes in chemical bonds and functional groups during the activation of H_2O_2 on Pd aerogels and $Pd_{100}Bi_5$ aerogels [31,32]. The surface of the Pd aerogels displays distinct peaks at 1,230 and 1,650 cm^{-1}, which can be attributed to the bending vibrations of •OH and H_2O, respectively. In $Pd_{100}Bi_5$ aerogels, the

H_2O bending vibrational peak is importantly enhanced, indicating a higher efficiency of activated H_2O_2. It is noteworthy that, in comparison to Pd aerogels, a bending vibration peak of the O–O bond at 1,125 cm^{-1} is observed in PdBi aerogels. This suggests that the PdBi aerogels effectively promote the polarized elongation of the O–O bond, thereby facilitating the activation of H_2O_2 for •OH generation (Fig. S11) [33]. To determine the proportion of •OH, a series of scavengers, including *tert*-butyl alcohol (TBA, •OH scavengers) and dimethylsulfoxide (DMSO, both •OH and metal-oxo species scavengers), are introduced into the H_2O_2 activation process system [34,35].

As depicted in Fig. S12 and Fig. 3E, the inhibitory effects of TBA and DMSO on the activation of H_2O_2 by $Pd_{100}Bi_5$ are similar, indicating that $Pd_{100}Bi_5$ mainly activates H_2O_2 to generate •OH. In contrast to $Pd_{100}Bi_5$, in the Pd system for H_2O_2 activation, the inhibitory effect of DMSO is stronger than that of TBA, suggesting that in the Pd system, H_2O_2 generates •OH and metal-oxo. Further analysis suggests that $Pd_{100}Bi_5$ aerogels decreased metal-oxo selectivity from 23.3% to 1.70%, dramatically increasing the •OH selectivity from 76.7% to 98.3%. Using benzoic acid (BA) as the probe molecule, a specific hydroxylation reaction converts BA into *p*-hydroxybenzoic acid. We observe that the concentration of •OH in the Pd system is 81.18 μmol/l, while the production of •OH in the $Pd_{100}Bi_5$ system increased to 314.07 μmol/l. Compared with Pd (73.3%), $Pd_{100}Bi_5$ (95.4%) importantly enhances the selectivity of •OH during the activation of H_2O_2 (Fig. S13 and Fig. 3F and G). This result is basically consistent with the results of the quenching experiment with the scavenger. In summary, $Pd_{100}Bi_5$ aerogels can selectively activate H_2O_2 to produce •OH and enhance H_2O_2 activation ability (Fig. 3H). Additionally, the stability of $Pd_{100}Bi_5$ aerogels is assessed. $Pd_{100}Bi_5$ aerogels have excellent tolerance and heat resistance (Figs. S14 and S15). Furthermore, the cyclic stability test demonstrates that after 10 cycles, the $Pd_{100}Bi_5$ aerogels still maintained excellent activity (Fig. S16). To further verify the structural integrity and chemical stability of the $Pd_{100}Bi_5$ after the reaction, we conduct a series of characterization tests on the nanozyme after the reaction. The TEM and x-ray diffraction results show that the $Pd_{100}Bi_5$ aerogel after the reaction still maintains its original porous framework structure and crystal phase composition, which is consistent with the state before the reaction (Fig. S17A to C). The XPS analysis indicated that the surface electronic states of Pd and Bi did not undergo important changes, indicating that the chemical state of the catalyst was maintained during the reaction process (Fig. S17D and E). Additionally, inductively coupled plasma tests on the supernatant after the reaction did not detect any leakage of Pd ions or Bi ions, further ruling out the possibility of the active components leaching out during the reaction. The above results collectively confirm that the $Pd_{100}Bi_5$ aerogel has excellent structural and chemical stability under catalytic reaction conditions (Table S4).

Intermolecular orbital hybridization between the Pd atom in PdBi and H_2O_2

To further clarify the mechanism of H_2O_2 activation and explain the outstanding catalytic performance of $Pd_{100}Bi_5$ aerogels, we propose a cascade hybridization model (p–d–σ), involving site 2 (p-block), site 1 (d-block), and hydrogen peroxide (σ). By precisely controlling the p–d orbital hybridization between sites 1 and 2, specific orbital coupling is expected to be achieved in the subsequent cascade hybridization. Firstly, given that HR-TEM and SAED images confirm (111) as the dominant exposed facet in the Pd and PdBi aerogels, we employ the Pd(111) surface as a representative model to investigate the effect of Bi doping on the electronic structure and adsorption energetics (Fig. S18). Due to the strong orbital hybridization between the d orbitals of Pd and the p orbitals of Bi, the d orbitals of Pd after hybridization have a greater degree of overlap with the bonding and antibonding orbitals when hybridizing with H_2O_2 (Fig. 4B and Fig. S19). Specifically, the energy levels of the $4d_z^2$ and $4d_{xz/yz}$ orbitals of Pd atoms in $Pd_{100}Bi_5$ are higher than those in Pd aerogels after p–d hybridization. Therefore, when the 4d orbitals of Pd in $Pd_{100}Bi_5$ interact with the 5σ and 2π* orbitals of H_2O_2, the energy of the antibonding orbitals is higher than that in Pd. This results in an increased electron occupancy of the bonding orbitals, thereby strengthening the adsorption interaction of H_2O_2 on $Pd_{100}Bi_5$ and weakening it on Pd (Fig. 4C and D) [36,37]. Further hybridization between Pd ($4d_z^2$, $4d_{xy}$, and $4d_{yz}$) and H_2O_2 (5σ and 2π*) in $Pd_{100}Bi_5$ aerogels is referred to as cascade orbital hybridization, which can achieve highly efficient and selective activation of H_2O_2 into •OH. Furthermore, to verify the role of the cascade orbital hybridization in the selectivity and efficiency of H_2O_2 activation, the lengths of H_2O_2 adsorbed on the surfaces of $Pd_{100}Bi_5$ aerogels and Pd aerogels were also calculated. To be specific, the O–O bonding length of the adsorbent of H_2O_2 (1.508 Å) on PdBi aerogels is longer, while the adsorbent of the O–O bonding length of H_2O_2 (1.489 Å) on Pd is shorter (Fig. 4E). Therefore, compared with Pd aerogels, $Pd_{100}Bi_5$ aerogels are more conducive to the selective generation of •OH from O–O bond breaking in H_2O_2. In addition, as shown in Fig. 4F and Fig. S20, the activation process and energy-change diagram of H_2O_2 on the $Pd_{100}Bi_5$ aerogels and Pd aerogels are presented. Firstly, the free energy of $*H_2O_2$ on $Pd_{100}Bi_5$ aerogels is significantly lower than that on Pd aerogels, which can promote H_2O_2 adsorption and match well with the PDOS analysis, providing evidence for promoting H_2O_2 activation through cascade orbital hybridization. Besides, $*H_2O_2$ is cleaved into 2 adsorbed *OH on Pd and Bi sites. Next, *OH is protonated to form $*H_2O$. Finally, $*H_2O$ is desorbed in succession, and the $Pd_{100}Bi_5$ aerogels return to the initial state. In this reaction, the step from *OH and $*H_2O$ to *OH can be regarded as the rate-determining step. The energy barrier for the rate-determining step of $Pd_{100}Bi_5$ aerogels (1.279 eV) is lower than that of Pd aerogels (1.543 eV), which is attributed to the redistribution of the electronic structure after the hybridization of $Pd_{100}Bi_5$ aerogels and H_2O_2 cascade orbitals. After the occurrence of the cascade orbital hybridization, the d-band center of Pd in the $Pd_{100}Bi_5$ aerogels (−2.42 eV) is lowered relative to the d-band center of pure Pd aerogels (−1.23 eV), which is conducive to the desorption of water molecules on the $Pd_{100}Bi_5$ aerogels (Fig. 4G). In summary, the p–d orbital hybridization interaction between Pd and Bi plays a crucial role in amplifying the cascade orbital hybridization process between Pd and H_2O_2. This interaction promotes the cascade orbital hybridization between Pd and H_2O_2, leading to the redistribution of electrons on the surface of the Pd aerogels, thereby facilitating the cleavage of the O–O bond during H_2O_2 activation and the effective removal of H_2O. As a result, this cascade orbital hybridization importantly enhances the selectivity and efficiency of H_2O_2 activation.

Identification of different pesticide residues

In agriculture, various pesticides, including organophosphorus, organochlorine, carbamates, phenol carboxylic acids, and sulfonamides, are widely used as growth regulators. However, the

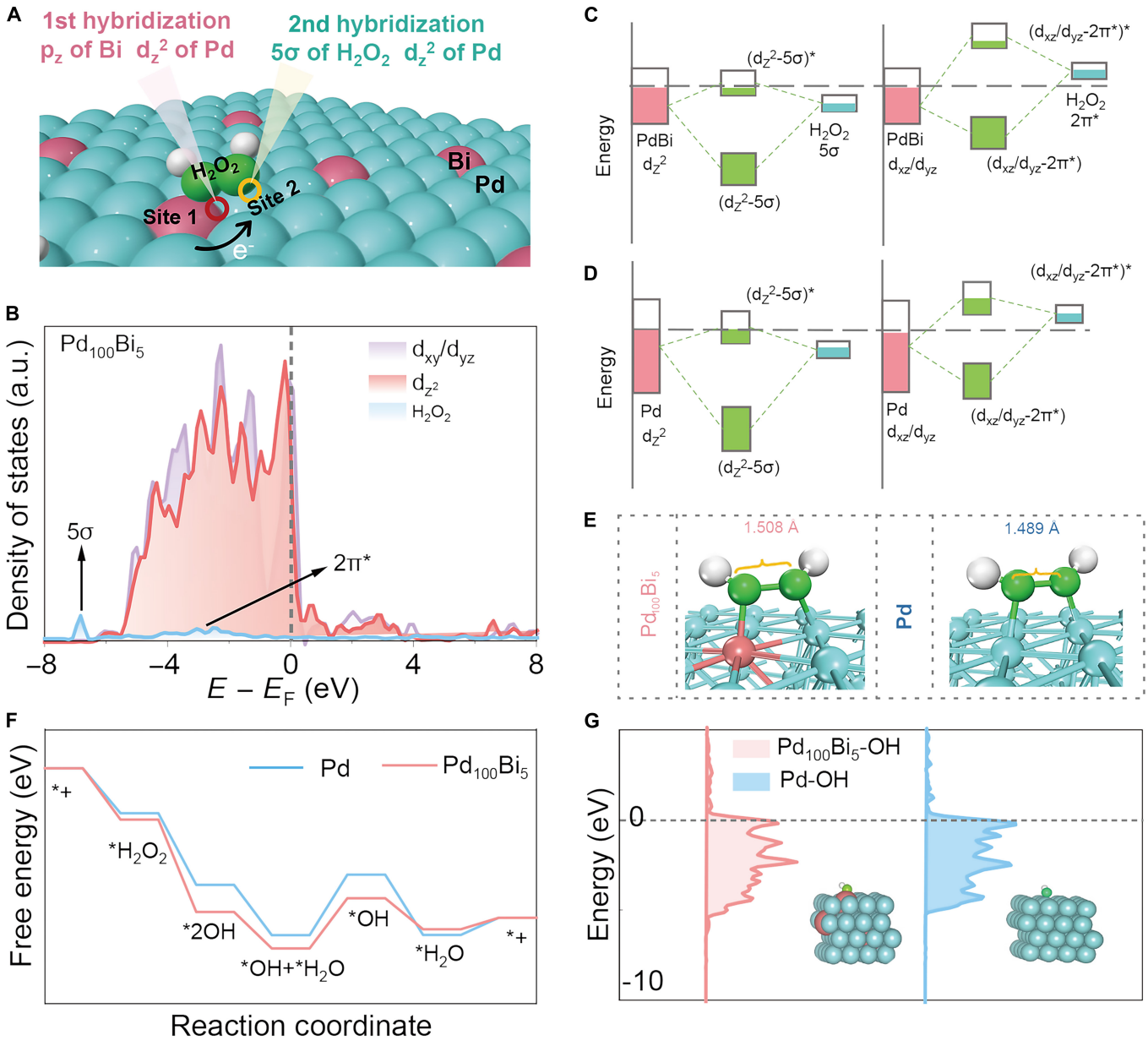


Fig. 4. (A) Schematic illustration of orbital interactions between H_2O_2 (5σ and 2π*) and 4d orbital for (B) $Pd_{100}Bi_5$ aerogels. (B) The DOS for Pd 4d $d_{xy}/d_{yz}/d_z^2$ orbitals and adsorbed H_2O_2 for $Pd_{100}Bi_5$ aerogels. Schematic illustration of orbital interactions between H_2O_2 (5σ and 2π*) and 4d orbital for (C) $Pd_{100}Bi_5$ and (D) Pd aerogels. (E) Structures of adsorbed H_2O_2 on Pd aerogels and $Pd_{100}Bi_5$ aerogels. (F) The energy-change diagram of the H_2O_2 reduction process on Pd aerogels and $Pd_{100}Bi_5$ aerogels. (G) The center of the d orbital of Pd after hybridization with the H_2O_2 cascade orbitals. Blue, red, white, and green spheres in the insets represent Pd, Bi, H, and O atoms, respectively.

incomplete degradation of these pesticides leads to residues that pose important threats to food safety. Therefore, simultaneously detecting and differentiating pesticides with diverse structures and properties remains a key scientific issue that urgently needs to be addressed [38–43]. To address this issue, a novel sensing strategy based on the catalytic inhibition effect has been developed. This strategy enables differential recognition of various pesticide types (e.g., organophosphorus, organochlorine, and carbamate) by precisely modulating the interactions between pesticide molecules and the nanozyme's active sites. Specifically, it shows a gradient inhibition effect on the activation process of H_2O_2 and the generation efficiency of •OH, thereby establishing a quantitative structure–activity relationship between the degree of inhibition and the type and concentration of pesticides.

For instance, organophosphorus pesticides like chlorpyrifos (CPF) strongly adsorb onto the nanozyme surface, importantly suppressing •OH production, while other pesticides (e.g., sulfonamides or phenolic acids) exhibit weaker inhibitory effects. By capturing these varying inhibition signals, the sensor array translates them into distinct response patterns, thereby enabling the detection of different pesticide residues. CPF is employed as a representative model for pesticide molecules. As illustrated in Fig. 5A, the XPS analysis reveals that the peak of Pd 3d shifts importantly with the addition of CPF, indicating an interaction between $Pd_{100}Bi_5$ aerogels and CPF [44,45]. This finding

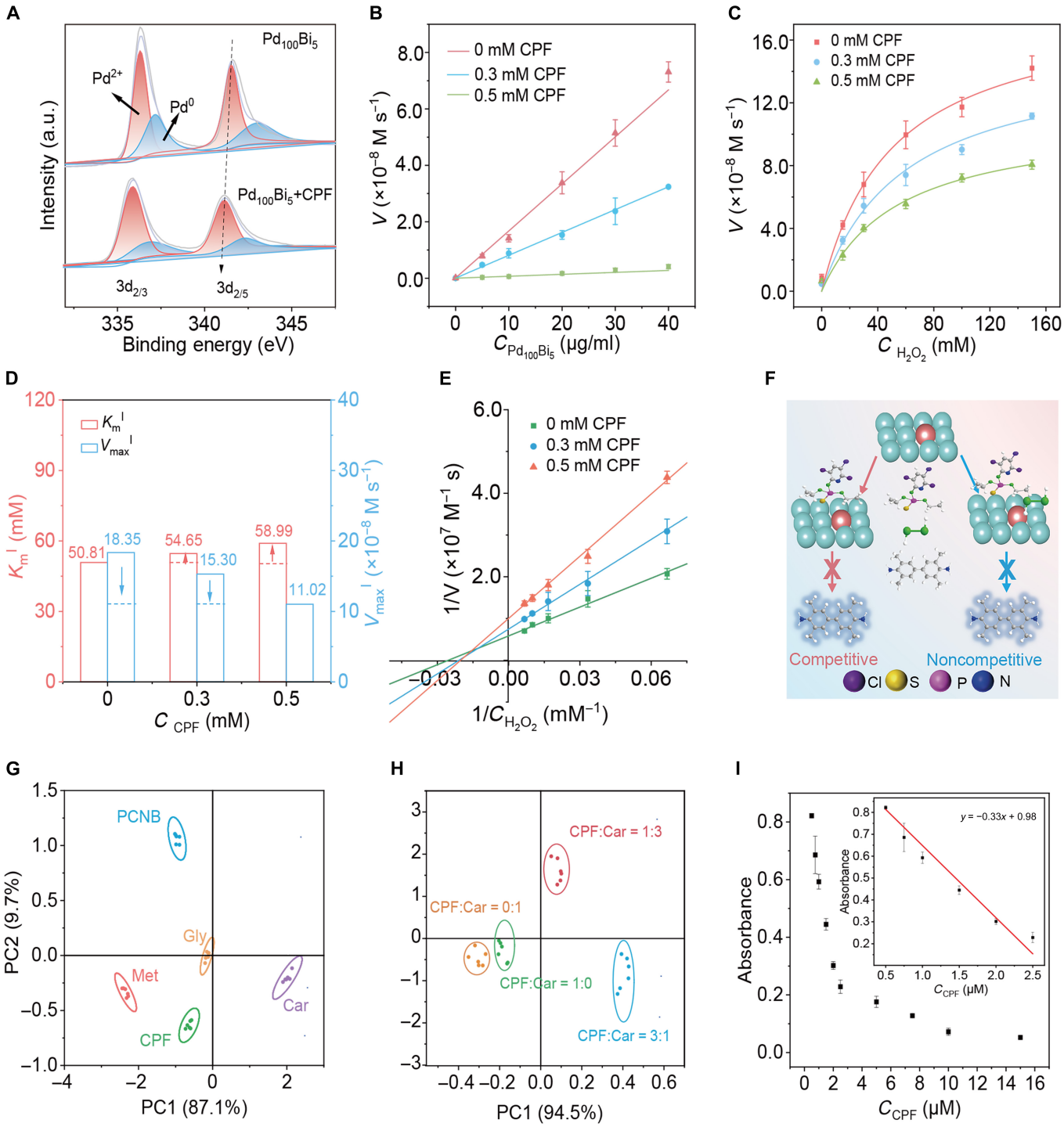


Fig. 5. (A) XPS spectra of Pd 4d for $Pd_{100}Bi_5$ aerogels and $Pd_{100}Bi_5$ aerogels + chlorpyrifos (CPF). (B) The initial velocities at different CPF concentrations vary with the $Pd_{100}Bi_5$ aerogel concentration. (C) Michaelis–Menten curves of $Pd_{100}Bi_5$ aerogels toward various concentrations of H_2O_2 at different CPF concentrations. (D) The V_{max}^{I} and K_m^{I} values of $Pd_{100}Bi_5$ aerogels in the presence of different concentrations of CPF. (E) Lineweaver–Burk plots of $Pd_{100}Bi_5$ aerogels toward various concentrations of H_2O_2 to varying concentrations of CPF. (F) Schematic diagram of the inhibition types of CPF on $Pd_{100}Bi_5$ aerogels. (G) Two-dimensional (2D) canonical score plots derived from the colorimetric sensor array responses to pentachloronitrobenzene (PCNB), metsulfuron-methyl (Met), glyphosate (Gly), carbaryl (Car), Chipton, and CPF. (H) 2D canonical score plots of the sensor array in response to binary pesticide mixtures with different molar ratios. (I) Linear ranges of the detection result from CPF.

highlights the need for further exploration into the inhibitory effects of CPF on $Pd_{100}Bi_5$ aerogels [27,46,47]. As shown in Fig. 5B, it can be seen that the rate of H_2O_2 activation exhibits a linear relationship with the concentration of $Pd_{100}Bi_5$ aerogels. As CPF increases, the slope of the line through the origin decreases, indicating that CPF reversibly inhibits the ability of $Pd_{100}Bi_5$ aerogels to activate H_2O_2. We additionally determine the initial velocity at various H_2O_2 concentrations in the presence of CPF, and the catalytic kinetics align with the Michaelis–Menten curve equation (Fig. 5C and Table S5). In the presence

of the inhibitor CPF, the Michaelis–Menten constant is denoted as K_m^I (inhibited state), while the maximum initial velocity is represented as V_{max}^I. With the increase of CPF concentration, K_m^I increased and V_{max}^I decreased (Fig. 5D). Moreover, Lineweaver–Burk plots constructed at various concentrations of CPF crossed in the second quadrant. This suggests that the inhibition is of a mixed type, encompassing both competitive and noncompetitive inhibition (Fig. 5E). K_I and K_I' represent the inhibition constants of the nanozyme–inhibitor and nanozyme–substrate–inhibitor systems, respectively. K_I and K_I' are calculated to be 0.557 and 0.783 mM. $K_I < K_I'$ indicates that the affinity of CPF for $Pd_{100}Bi_5$ is higher than that of the complex formed by $Pd_{100}Bi_5$ and H_2O_2, further suggesting that competitive inhibition plays a dominant role in the mixed inhibition. In conclusion, CPF reduces the affinity of $Pd_{100}Bi_5$ aerogels for the substrate H_2O_2 through a mixed inhibition mode, thereby reducing the activation ability of H_2O_2 (Fig. 5F). To gain deeper insight into the molecular-scale interaction between CPF and the PdBi surface, density functional theory calculations were performed. The CPF molecule is modeled on the $Pd_{100}Bi_5$ surface, with the P=S functional group identified as the primary binding motif. The calculated adsorption energy of CPF on $Pd_{100}Bi_5$ is −0.45 eV, importantly stronger than that of H_2O_2 (−1.55 eV), indicating that CPF preferentially occupies the Pd active sites and competitively inhibits H_2O_2 activation. PDOS further shows pronounced orbital overlap between the Pd 4d orbitals and the S 3p orbitals of CPF near the Fermi level, providing direct evidence for orbital hybridization underlying the competitive inhibition mechanism (Fig. S21). In addition, other typical pesticides, including pentachloronitrobenzene (PCNB), carbaryl (Car), glyphosate (Gly), and metsulfuron-methyl (Met), are also discussed for their inhibition effects on the selective generation of •OH by activated H_2O_2. As shown in Fig. S22, PCNB, Car, Gly, and Met exhibit typical reversible inhibition features. According to the intersection position of the Lineweaver–Burk diagram (Fig. S23), the inhibition types of the above 5 pesticides can be determined (Table S6). Inspired by the results mentioned above, the extent of inhibition of H_2O_2 activation varied among different pesticide molecules, offering a promising approach to distinguish and identify multiple pesticides across diverse categories. Pd, $Pd_{100}Bi_2$, and $Pd_{100}Bi_5$ aerogels are utilized to construct a simple 3-channel sensor array. We employ sensor arrays for cross-reactive discrimination of various pesticides (CPF, PCNB, Car, Gly, and Met). Subsequently, through the application of principal component analysis for transforming the complex training-data matrix, 5 types of pesticides are effectively differentiated, resulting in tightly formed clusters (Fig. 5G). Additionally, the sensing arrays demonstrate the ability to precisely recognize mixtures of CPF and Car in various proportions (Fig. 5H). To provide a more robust and quantitative assessment of sensitivity, we perform conventional univariate calibration using the $Pd_{100}Bi_5$ aerogels that exhibit the highest response to CPF. As shown in Fig. 5I, the response intensity shows a linear relationship with CPF concentration in the range of 0.5 to 2.5 μM. The detection limit (0.23 μM) is calculated as 3σ/slope, where σ is the standard deviation of the blank measurements ($n = 10$). This detection limit is considerably lower than the maximum residue limits for CPF established by the European Union.

In the actual sample analysis experiment, simulated pesticide spraying is used to analyze pesticide residues on grape surfaces. Extracting solutions containing different types of pesticides as samples to be tested produces unique response signals. As shown in Fig. S24, the 2-dimensional canonical score plot shows that the 5 types of pesticides are separated into 5 distinct regions, clearly apart from each other, demonstrating excellent discriminating ability.

Conclusion

In summary, the integration of p-block metal Bi into Pd aerogels to form PdBi aerogels has been shown to importantly enhance the selective activation of H_2O_2 through the introduction of tensile strain. This strain leads to a subsequent enhancement of orbital hybridization between the d orbitals of Pd and the p orbitals of Bi. This change in orbital hybridization and energy levels facilitates the interaction between the Pd $4d_{xz/yz}$ and $4d_z^2$ orbitals and the $2\pi^*$ and 5σ orbitals of H_2O_2 molecules during H_2O_2 activation. Consequently, $Pd_{100}Bi_5$ aerogels exhibit reduced metal-oxo selectivity and markedly increased •OH selectivity, thereby improving the activation efficiency of H_2O_2. Leveraging these properties, a colorimetric sensor array has been developed to effectively distinguish and detect various types of pesticides. Furthermore, we expect that the cascade orbital hybridization strategy demonstrated here is expected to be extendable to other catalytic processes involving small-molecule activation, such as the oxygen reduction reaction and the oxygen evolution reaction, where tuning intermediate adsorption is critical.

Materials and Methods

Materials

$Pd(acac)_2$, $BiCl_3$, PCNB, Gly, CPF, Car, Met, Chipton, and horseradish peroxidase were purchased from Shanghai Aladdin Biochemical Technology Co., Ltd. Sodium acetate (NaAc), terephthalic acid, and TMB were obtained from Sinopharm Chemical Reagent Co., Ltd.

Preparation of Pd and PdBi aerogels

In a typical synthesis of PdBi aerogels, 2 ml of aqueous $NaBH_4$ (0.05 M) was quickly injected into 30 ml of an aqueous metal precursor solution containing 0.4 ml $Pd(acac)_2$ (0.1 M) and 0.04 ml $BiCl_3$ (0.05 M), with stirring at 60 °C. The prepared mixture solution was stirred at 600 rpm for 1 min and changed from faint yellow to black. Finally, the black solution was heated to 60 °C for 2 h to form PdBi aerogels. The black monolith solids were carefully washed with water 3 times and finally dried at −60 °C in the lyophilized chamber. Pd and PdBi aerogels were prepared with Pd and Bi source mole ratios of 100:0, 100:2, and 100:10 using the same process.

Evaluations of the activation properties of H_2O_2

The ability of Pd aerogels and PdBi aerogels to activate H_2O_2 was evaluated through a traditional colorimetric reaction, using TMB (a colorimetric agent) as an indicator in the presence of acetic acid–sodium acetate (HAc–NaAc) buffer and an aqueous H_2O_2 solution. Specifically, 5 μl of Pd aerogels or PdBi aerogels (0.05 mg/ml), 100 μl of H_2O_2 (100 mM) water solution, and 100 μl of TMB (1 mM) ethanol solution were sequentially added to 100 μl of HAc–NaAc buffer solution (pH 3.0, 0.1 M). Following a 2-min incubation period, the absorbance at 652 nm of the resulting mixture was measured using a multimode reader.

Construction of the colorimetric sensor array for pesticide identification

A colorimetric sensor array based on PdBi aerogels ($3 \times 6 \times 6$) was assembled in a 96-well plate. The detailed steps were as follows: HAc–NaAc, TMB, H_2O_2, 3 distinct types of PdBi aerogels, and pesticide standards at various concentrations were added into the 96-well plate. Following a 5-min incubation period, the absorbance of the solution was recorded at 652 nm using a microplate reader. This procedure was conducted 6 times for 6 different antioxidants. As a result, the antioxidants were evaluated using 3 types of PdBi aerogels, generating a $3 \times 6 \times 6$ data matrix.

Acknowledgments

Funding: The authors gratefully acknowledge the financial support from the National Natural Science Foundation of China (nos. 22304096 and 52470193), the project ZR2023QB006 supported by Shandong Provincial Natural Science Foundation, the Fundamental Research Funds for the Central Universities (no. CCNU24JCPT032), and the Qingdao Science and Technology Benefit Demonstration Project (no. 26-1-5-xdny-25-nsh).

Author contributions: R.L.: Writing—original draft, investigation, methodology, and formal analysis. C.C.: Writing—review and editing and investigation. L.H.: Writing—review and editing and formal analysis. D.Y.: Writing—review and editing. X.L.: Writing—review and editing. X.J.: Writing—review and editing. Y.W.: Writing—review and editing. L.J.: Conceptualization, writing—review and editing, supervision, and funding acquisition. Y.Z.: Writing—review and editing, supervision, and funding acquisition. C.Z.: Writing—review and editing, supervision, project administration, and funding acquisition.

Competing interests: The authors declare that they have no competing interests.

Data Availability

The data supporting this study's findings are available within the article and its supplementary materials.

Supplementary Materials

Figs. S1 to S24
Tables S1 to S6

References

1. Zhang C, Shan P, Zou Y, Bao T, Zhang X, Li Z, Wang Y, Wei G, Liu C, Yu C. Stable and high-yield hydrogen peroxide electrosynthesis from seawater. *Nat Sustain*. 2025;8(5):542–552.
2. Wu Y, Jiang W, Xu W, Lv F, Song S, Hu L, Wang C, Zheng L, Gu W, Zhang R, et al. Hydroxyl spillover in Fe–Se dual-site catalysts for mixed plastics assay. *J Am Chem Soc*. 2025;147(1):1356–1363.
3. Zhang Y-J, Tao J-S, Hu Y, Huang G-X, Pan Y, Li W-W, Chen J-J, Yu H-Q. Metal oxyhalide-based heterogeneous catalytic water purification with ultralow H_2O_2 consumption. *Nat Water*. 2024;2(8):770–781.
4. Jiang Z, Tong K, Li Z, Tao H, Zhu M. Spin state regulation for peroxide activation: Fundamental insights and regulation mechanisms. *Angew Chem Int Ed Engl*. 2025;64(16):Article e202500791.
5. Zhang S, Gao XJ, Ma Y, Song K, Ge M, Ma S, Zhang L, Yuan Y, Jiang W, Wu Z, et al. A bioinspired sulfur–Fe–heme nanozyme with selective peroxidase-like activity for enhanced tumor chemotherapy. *Nat Commun*. 2024;15(1):10605.
6. Kottaichamy AR, Marichelvam T, Tzadikov J, Vaza RC, Volokh M, Barzilai S, Shalom M. Energy-efficient hydrogen generation via peroxide-mediated electrocatalytic pathways. *Angew Chem Int Ed Engl*. 2025;64(28):Article e202502735.
7. Carlsson LM, Jonsson J, Edlund T, Marklund SL. Mice lacking extracellular superoxide dismutase are more sensitive to hyperoxia. *Proc Natl Acad Sci USA*. 1995;92(14):6264–6268.
8. Zhou Z, Zhao S, Li Z, Wang P, Zhan S, Wang M. Activating oxygen via the 3-electron pathway to hydroxyl radical by La–O_4 single-atom on WO_3 for water purification. *Angew Chem Int Ed Engl*. 2025;64(6):Article e202418122.
9. Xing M, Xu W, Dong C, Bai Y, Zeng J, Zhou Y, Zhang J, Yin Y. Metal sulfides as excellent co-catalysts for H_2O_2 decomposition in advanced oxidation processes. *Chem*. 2018;4(6):1359–1372.
10. Wu Y, Li J, Jiang W, Xu W, Zheng L, Wang C, Gu W, Zhu C. Second coordination sphere regulates nanozyme inhibition to assist early drug discovery. *Nat Commun*. 2025;16(1):3123.
11. Kang Z, Jiang J, Tu Q, Liu S, Zhang Y, Wang D-E, Wang J, Yuan M-S. Dual-site chemosensor for monitoring ·OH-cysteine redox in cells and in vivo. *J Am Chem Soc*. 2023;145(1):507–515.
12. Zhao G, Tao X, Guo T, Fu L, Yang H. Mineral-mediated epitaxial growth of CoO nanoparticles for efficient electrochemical H_2O_2 activation. *ACS Nano*. 2025;19(1):1509–1518.
13. Wang F, Gao Y, Chai Y, Wang C-C, Wang J-F, Yi X-H, Li Y, Fu H, Zhao C, Wang P. Interfacial engineering regulating electronic structure of homologous S-scheme Co_3O_4@C-TiO_2 heterojunction for enhanced Fenton-like reaction activity. *Appl Catal B Environ*. 2025;364:Article 124848.
14. Liu C, Shi W, Yuan Y, Zhu K, Zhang Q, Li S, Yang X, Bai Z, Yang L. Cascade hydrogen peroxide reduction reaction endows Cu-Fe dual-atom catalyst with durable oxygen reduction performance. *Adv Funct Mater*. 2025;35(35):Article 2503079.
15. Ma S, Dong B, Zheng Y, Tang S, Zhang T, Zhao Y. Dual-substrate synergistic catalysis of WS_2-Fe clusters on recycled plastic-derived N-doped carbon for H_2O_2 activation. *Appl Catal B Environ*. 2025;377:Article 125522.
16. Zhang R, Xue B, Tao Y, Zhao H, Zhang Z, Wang X, Zhou X, Jiang B, Yang Z, Yan X, et al. Edge-site engineering of defective Fe-N_4 nanozymes with boosted catalase-like performance for retinal vasculopathies. *Adv Mater*. 2022;34(39):2205324.
17. Zhang X, Zhang Y, Tian J, Guo Y, Zhou Z, Liu Z, Zhao Z, Liu B, Li J. Generating $^1O_2$ and Co^{IV}=O through efficient peroxymonosulfate activation by $ZnCo_2O_4$ nanosheets for pollutant control. *Nano Res*. 2024;17(9):8025–8035.
18. Chen C, Yan D, Jia X, Li R, Hu L, Li X, Jiao L, Zhu C, Zhai Y, Lu X. Oxygen-bridged W-Pd atomic pairs enable H_2O_2 activation for sensitive immunoassays. *Chem Sci*. 2024;15(37):15440–15447.
19. Tang Y, Chen Y, Wu Y, Xu W, Luo Z, Ye H-R, Gu W, Song W, Guo S, Zhu C. High-indexed intermetallic Pt_3Sn nanozymes with high activity and specificity for sensitive immunoassay. *Nano Lett*. 2023;23(1):267–275.
20. Zhou Y, Gu Q, Yin K, Tao L, Li Y, Tan H, Yang Y, Guo S. Cascaded orbital–oriented hybridization of intermetallic

Pd_3Pb boosts electrocatalysis of Li-O_2 battery. *Proc Natl Acad Sci USA*. 2023;120(25):Article e2301439120.
21. Wu J, Zhu X, Li Q, Fu Q, Wang B, Li B, Wang S, Chang Q, Xiang H, Ye C, et al. Enhancing radiation-resistance and peroxidase-like activity of single-atom copper nanozyme via local coordination manipulation. *Nat Commun*. 2024;15(1):6174.
22. Jiang Y, Deng Y-P, Liang R, Fu J, Gao R, Luo D, Bai Z, Hu Y, Yu A, Chen Z. d-Orbital steered active sites through ligand editing on heterometal imidazole frameworks for rechargeable zinc-air battery. *Nat Commun*. 2020;11(1):5858.
23. Wang Y, Tang H, Feng H, Chai D-F, Zhang W, Han X, Li Y, Dong G, Guo D. d-d orbital interactions and spin-state modulation drive extensive surface reconstruction in chromium-incorporated layered double hydroxides for enhanced electrocatalytic oxygen evolution. *Appl Catal B Environ*. 2025;379:Article 125681.
24. Chen L, Yang Z, Hu Q, Yan C, Yao Y, Bao Y, Pei Z, Mu T, Xue Z. Engineering gradient d-d orbital occupancy to boost substrate adsorption for efficient electrocatalytic biomass valorization. *Angew Chem Int Ed Engl*. 2025;64(42): Article e202511868.
25. Fan X, Zerebecki S, Du R, Hübner R, Marzum G, Jiang G, Hu Y, Barcikowki S, Reichenberger S, Eychmüller A. Promoting the electrocatalytic performance of noble metal aerogels by ligand-directed modulation. *Angew Chem Int Ed Engl*. 2020;59(14):5706–5711.
26. Wang H, Zheng H, Ling L, Fang Q, Jiao L, Zheng L, Qin Y, Luo Z, Gu W, Song W, et al. Pd metallene aerogels with single-atom W doping for selective ethanol oxidation. *ACS Nano*. 2022;16:21266–21274.
27. Chen J, Zhang F, Kuang M, Wang L, Wang H, Li W, Yang J. Unveiling synergy of strain and ligand effects in metallic aerogel for electrocatalytic polyethylene terephthalate upcycling. *Proc Natl Acad Sci USA*. 2024;121(17): Article e2318853121.
28. Jia X, Jiao L, Li R, Yan D, Hu L, Chen C, Li X, Zhai Y, Lu X. Inhibition effect of p-d orbital hybridized PtSn nanozymes for colorimetric sensor array of antioxidants. *Biosens Bioelectron*. 2024;261:Article 116468.
29. Qin Z, Jiao L, Hu L, Zhang Y, Jia X, Chen C, Sun X, Zhai Y, Zhu Z, Lu X. Amorphous RuO_2 nanozymes with an excellent catalytic efficiency superior to natural peroxidases. *Small*. 2025;21(24):Article e2502158.
30. Sha M, Rao L, Xu W, Qin Y, Su R, Wu Y, Fang Q, Wang H, Cui X, Zheng L, et al. Amino-ligand-coordinated dicopper active sites enable catechol oxidase-like activity for chiral recognition and catalysis. *Nano Lett*. 2023;23(2):701–709.
31. Sheng H, Zhang H, Song W, Ji H, Ma W, Chen C, Zhao J. Activation of water in titanium dioxide photocatalysis by formation of surface hydrogen bonds: An in situ IR spectroscopy study. *Angew Chem Int Ed Engl*. 2015;54(20):5905–5909.
32. Wu Y, Wen J, Xu W, Huang J, Jiao L, Tang Y, Chen Y, Yan H, Cao S, Zheng L, et al. Defect-engineered nanozyme-linked receptors. *Small*. 2021;17(33):2101907.
33. Mondal S, Bagchi D, Riyaz M, Sarkar S, Singh AK, Vinod CP, Peter SC. In situ mechanistic insights for the oxygen reduction reaction in chemically modulated ordered intermetallic catalyst promoting complete electron transfer. *J Am Chem Soc*. 2022;144(26):11859–11869.
34. Malik DD, Ryu W, Kim Y, Singh G, Kim J-H, Sankaralingam M, Lee Y-M, Seo MS, Sundararajan M, Ocampo D, et al. Identification, characterization, and electronic structures of interconvertible cobalt-oxygen TAML intermediates. *J Am Chem Soc*. 2024;146(20):13817–13835.
35. Xiao F, Wang Z, Fan J, Majima T, Zhao H, Zhao G. Selective electrocatalytic reduction of oxygen to hydroxyl radicals via 3-electron pathway with FeCo alloy encapsulated carbon aerogel for fast and complete removing pollutants. *Angew Chem Int Ed Engl*. 2021;60(18):10375–10383.
36. Jing Q, Mei Z, Sheng X, Zou X, Xu Q, Wang L, Guo H. Tuning the bonding behavior of d-p orbitals to enhance oxygen reduction through push-pull electronic effects. *Adv Funct Mater*. 2024;34(3):2307002.
37. Zhou Y, Chen J, Sun J, Zhao T. Engineering the d-orbital energy of metal-organic frameworks-based solid-state electrolytes for lithium-metal batteries. *Nano Lett*. 2024;24(6):2033–2040.
38. Valcke M, Bourgault M-H, Rochette L, Normandin L, Samuel O, Belleville D, Blanchet C, Phaneuf D. Human health risk assessment on the consumption of fruits and vegetables containing residual pesticides: A cancer and non-cancer risk/benefit perspective. *Environ Int*. 2017;108:63–74.
39. Qian S, Lin H. Colorimetric sensor array for detection and identification of organophosphorus and carbamate pesticides. *Anal Chem*. 2015;87(10):5395–5400.
40. Song D, Zou Y, Tian T, Ma Y, Huang H, Li Y. Machine learning-assisted melamine-Cu nanozyme and cholinesterase integrated array for multi-category pesticide intelligent recognition. *Biosens Bioelectron*. 2024;266:Article 116747.
41. Bai Y, Nie S, Gao W, Li N, Zhu P, Zhang L, Yu J. Enzyme-nanozyme cascade flow reactor synergy with deep learning for differentiation and point-of-care testing of multiple organophosphorus pesticides. *Adv Funct Mater*. 2025;35(17):2419499.
42. Yan X, Wang T, Li H, Zhang L, Xin H, Lu G. Flexible aggregation-induced emission-active hydrogel for on-site monitoring of pesticide degradation. *ACS Nano*. 2022;16(11):18421–18429.
43. Song D, Tian T, Wang L, Zou Y, Zhao L, Xiao J, Huang H, Li Y. Multi-signal sensor array based on a fluorescent nanozyme for broad-spectrum screening of pesticides. *Chem Eng J*. 2024;482:Article 148784.
44. Hu L, Li R, Chen C, Jia X, Li X, Jiao L, Zhu C, Lu X, Zhai Y, Guo S. Cu single sites on BO_2 as thyroid peroxidase mimicking for iodotyrosine coupling and pharmaceutical assess. *Sci Bull*. 2025;70(10):1611–1618.
45. Xu Y, Xue J, Zhou Q, Zheng Y, Chen X, Liu S, Shen Y, Zhang Y. The Fe-N-C nanozyme with both accelerated and inhibited biocatalytic activities capable of accessing drug–drug interactions. *Angew Chem Int Ed Engl*. 2020;59(34):14498–14503.
46. Wu W, Huang L, Zhu X, Chen J, Chao D, Li M, Wu S, Dong S. Reversible inhibition of the oxidase-like activity of Fe single-atom nanozymes for drug detection. *Chem Sci*. 2022;13(16):4566–4572.
47. Yan D, Wang C, Jia X, Chen C, Hu L, Zhai Y, Strizhak PE, Tang J, Jiao L, Zhu Z. Inhibition effect-involved colorimetric sensor array based on PtBi aerogel nanozymes for discrimination of antioxidants. *Food Chem*. 2025;478:Article 143729.